Research Article

Aneesh Bapat, Saurabh Dixit, Yashika Gupta, Tony Low and Anshuman Kumar*

Gate tunable light–matter interaction in natural biaxial hyperbolic van der Waals heterostructures

Abstract: The recent discovery of natural biaxial hyperbolicity in van der Waals crystals, such as α-MoO$_3$, has opened up new avenues for mid-IR nanophotonics due to their deep subwavelength phonon polaritons. However, a significant challenge is the lack of active tunability of these hyperbolic phonon polaritons. In this work, we investigate heterostructures of graphene and α-MoO$_3$ for actively tunable hybrid plasmon phonon polariton modes via electrostatic gating in the mid-infrared spectral region. We observe a unique propagation direction dependent hybridization of graphene plasmon polaritons with hyperbolic phonon polaritons for experimentally feasible values of graphene chemical potential. We further report an application to tunable valley quantum interference in this system with a broad operational bandwidth due to the formation of these hybrid modes. This work presents a lithography-free alternative for actively tunable, anisotropic spontaneous emission enhancement using a sub-wavelength thick naturally biaxial hyperbolic material.

Keywords: biaxial hybrid plasmon phonon polariton; graphene; in-plane hyperbolic materials; quantum interference; valleytronics; van der Waals heterostructures.

1 Introduction

Two-dimensional materials [1, 2] have enabled new avenues for quantum photonics [3] due to their potential for strong confinement of free space radiation at the deep sub-wavelength scale. The extreme confinement of electromagnetic waves and consequently strong light–matter interaction arises from polaritons [1, 2] – quasiparticles formed by the hybridization of a photon with charged dipolar excitations such as plasmon (for plasmon polaritons (PPs)) or lattice vibrations (for phonon polaritons (PhPs)). Extensive research on van der Waals (vdW) crystals [2, 4, 5], supporting PhPs and PPs, have demonstrated inherent hyperbolic anisotropy, that is, the permittivity being negative in one direction and positive in the other, and their applications in various nanophotonic devices such as infrared optical components [6–8], thermal emitters [9], enhanced spontaneous emission rate (SER) [10], and others [11]. In particular, anisotropic spontaneous emission rate [12, 13], associated with Purcell effect [14], has great relevance for applications to light sources [10, 15], quantum interference [13, 16], Kerr non-linearity enhancement [17], selective coupling to dark and bright excitons and others [18, 19].

Traditionally, hyperbolic anisotropy is achieved by complex lithographic techniques where carefully engineered sub-wavelength nanostructure of metal/dielectric materials acts like an elemental unit to attain hyperbolic dielectric permittivity tensor [20]. However, this approach relies on effective medium theory where typically close to resonances, the interaction between neighbouring units cells becomes important leading to a non-local response [21]. Moreover, the maximum possible wave-vector in these systems is limited by the size of the constituent unit cell, which is limited by fabrication constraints [22]. Lastly, artificial HMMs mostly rely on plasmonic constituent materials for the unit cells, which inevitably leads to high Ohmic losses [1, 22]. Such problems can be easily overcome via natural hyperbolic materials. Hence naturally hyperbolic vdW materials are an excellent alternative to artificially engineered systems. However, the tunability and anisotropy of these polaritons, particularly, PhPs over large operational bandwidth in conventional vdW materials [2] are major limitations for applications.

Graphene has been shown to be an excellent platform for tunable SPPs via electrostatic gating over a broad

---

*Corresponding author: Anshuman Kumar, Laboratory of Optics of Quantum Materials, Physics Department, IIT Bombay, Mumbai 400076, India, E-mail: anshuman.kumar@iitb.ac.in. https://orcid.org/0000-0002-7433-8341
Aneesh Bapat, Saurabh Dixit and Yashika Gupta, Laboratory of Optics of Quantum Materials, Physics Department, IIT Bombay, Mumbai 400076, India. https://orcid.org/0000-0003-4035-5343 (S. Dixit)
Tony Low, Department of Electrical and Computer Engineering, University of Minnesota, Minneapolis, MN 55455, USA

spectral region [23, 24], however, these SPPs are associated with optical losses [25]. On the contrary, hyperbolic PhPs are relatively long lived but are restricted within a narrow spectral bandwidth [26]. To this end, the integration of graphene with h-BN [27–29] and other dielectric crystals [30, 31] has shown gate-voltage tunable hybrid plasmon-phonon polaritons (HPPPs). The HPPP modes provide anisotropic propagation of polaritons [29] up to 2 times longer distances than hyperbolic PhPs [32] with reduced damping [27]. Several interesting applications have also been demonstrated using these HPPPS in uniaxial crystals [33–35]. However, there exists a wide spectral gap (400 cm^{-1} to 1100 cm^{-1}) and uniaxial anisotropic h-BN crystal exhibits narrow Reststrahlen Bands (RBs) – spectral region between LO and TO phonons of a particular polarization. Furthermore, the in-plane anisotropy of SERs for heterostructure of graphene with other hyperbolic materials like h-BN and LiNbO$_3$ is further restricted by their uniaxial nature [28, 30, 31]. This challenge can be addressed via recently discovered natural vdW crystal [4], i.e. α-MoO$_3$, which exhibits biaxial hyperbolic anisotropy in the mid-infrared spectral region from 545 cm^{-1}–1006 cm^{-1}. Therefore, integration of graphene with α-MoO$_3$ can provide highly anisotropic polarization dependent SERs over a broad spectral region without using any complex lithography techniques. Our proposed platform can enhance the emission from inter-band transition based mid-IR and far-IR sources [36–39].

In this work, we present a natural platform for tunable anisotropic HPPPs over a broad spectral region (from 545 cm^{-1}–1100 cm^{-1}) via integration of graphene with biaxial hyperbolic vdW crystal, i.e. α-MoO$_3$, shown in Figure 1. We theoretically investigate optical properties of air/graphene/α-MoO$_3$/Si heterostructure using the transfer matrix method (TMM) [40] as a function of chemical potential of graphene. Furthermore, we develop a theoretical framework by combining TMM with Green's dyadic function [41–43] to investigate anisotropic SERs from an electric dipole in the vicinity of the proposed heterostructure. We found that the coupling of graphene SPPs with hyperbolic PhPs of α-MoO$_3$ results in remarkably enhanced SERs over a broad mid-IR spectral region. This investigation provides a lithography-free alternative for actively tunable anisotropic SERs via a sub-wavelength thick crystal of naturally biaxial hyperbolic materials. As an example application, we present our results on gate tunable spontaneous valley coherence [16, 44, 45], quantified by quantum interference, using this heterostructure platform.

2 Results and discussion

2.1 Biaxial hyperbolic phonon polaritons in α-MoO$_3$

The α-MoO$_3$ unit cell has lattice constants of around 0.396 nm, 0.369 nm and 1.385 nm in the x, y and z crystallographic directions [4] as shown in Figure 1(a). The orthorhombic nature of the unit cell results in different sets of longitudinal optical (LO) and transverse optical (TO)
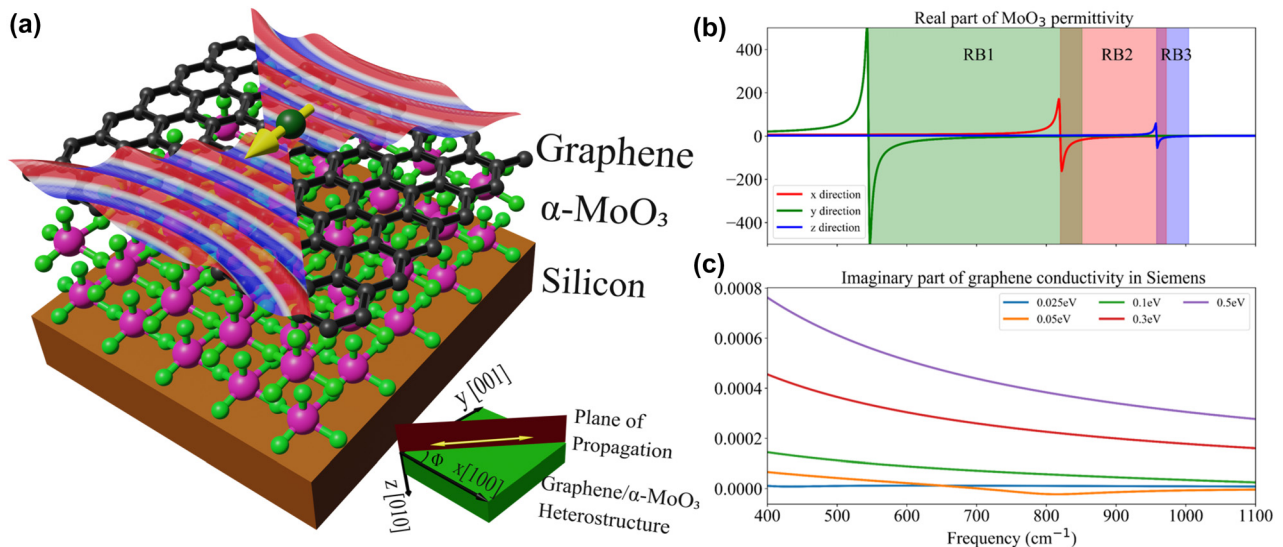

Figure 1: (a) Schematic representation of α-MoO$_3$ and graphene heterostructure on silicon substrate exhibiting the hybrid plasmon-phonon polariton modes propagation at the surface. Inset: crystallographic direction of α-MoO$_3$ and ϕ – angle between plane of propagation of light and x-axis of the α-MoO$_3$. (b) Real component of dielectric permittivity of α-MoO$_3$ along the principal directions. (c) Imaginary component of 2D in-plane conductivities for varying chemical potential in graphene.

phonons in the three crystallographic directions. The three sets of LO and TO phonons constitute three RBs in the mid-infrared spectral region, where α-MoO$_3$ exhibits natural biaxial hyperbolicity. Spectral region for RB-1, RB-2 and RB-3 of α-MoO$_3$ lie in the ranges of 545 cm^{-1}–850 cm^{-1}, 820 cm^{-1}–972 cm^{-1}, and 958 cm^{-1}–1006 cm^{-1}, respectively, where real part of dielectric permittivity is negative along y, x and z crystallographic directions, respectively, as shown in Figure 1(b) [46]. Since α-MoO$_3$ is a biaxial hyperbolic material, the dispersion of PhPs strongly depends on angle between plane of propagation of the polaritons and x-crystallographic direction as shown in Figure 1(a) and represented by ϕ. We investigate the dispersion of PhPs in

an air/α-MoO$_3$/Si heterostructure at ϕ = 0°, 45° and 90° as shown in Figure 2(a)–(c). Here, the thickness of α-MoO$_3$ is chosen to be 50 nm, and the imaginary part of the Fresnel reflection coefficient for p-polarized light is plotted in frequency-momentum space.

Figure 2(a) reveals discrete modes in the RB-2 and RB-3 spectral regions for ϕ = 0°, which are attributed to the hyperbolic anisotropy of α-MoO$_3$ resulting in the dispersion of fundamental and higher-order modes of hyperbolic PhPs. These modes demonstrate positive dispersion (i.e., $v_g > 0$) in RB-2 spectral region (Type-2 hyperbolicity) and negative dispersion (i.e., $v_g < 0$) in RB-3 spectral region (Type-1 hyperbolicity). Negative dispersion in the RB-3
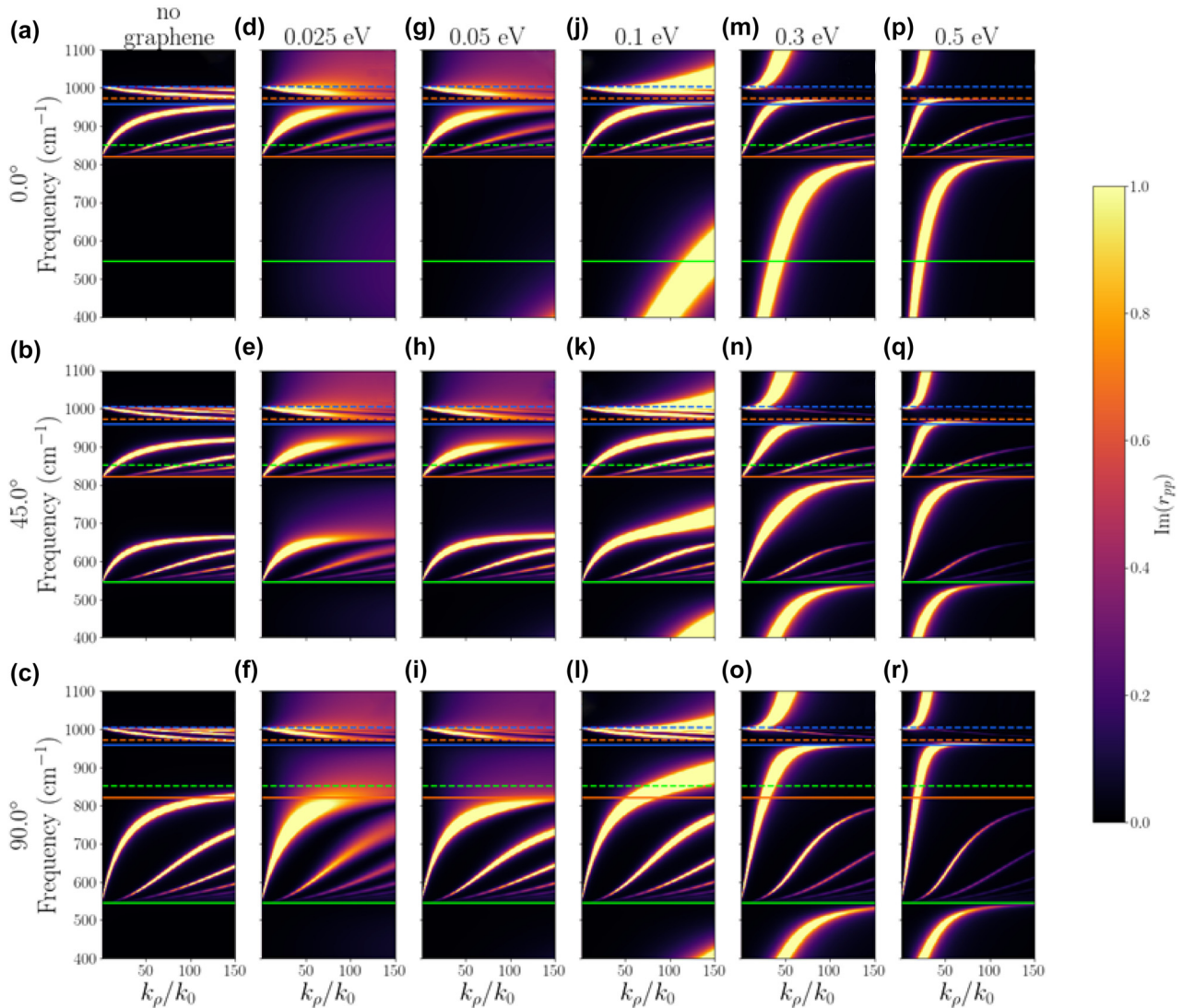
Figure 2: Dispersion of polaritonic modes in air/graphene/α-MoO$_3$ (50 nm)/Si heterostructure as a function of ϕ and chemical potential (μ) of graphene. Dotted lines indicate LO phonon frequencies, and solid lines indicate TO phonon frequencies along y-(green), x-(orange) and z-(blue) crystallographic directions of α-MoO$_3$. The color axis represents imaginary part of unitless quantity Fresnel's reflection coefficient for p-polarized light.

spectral region is associated with the negative real part of dielectric permittivity in the out-of-plane crystallographic direction. We also observe similar PhP modes for $\phi = 90°$ in the RB-1 and RB-3 regions (Figure 2(c)). For $\phi = 45°$ we observe Type-1 hyperbolic PhP modes in both RB1 and RB2 as the in-plane (ϵ_{11}, ϵ_{12}, ϵ_{21}, ϵ_{22}) entries of the rotated permittivity tensor depend on the permittivity along both x and y principal directions. However, these modes do not span the entire frequency range of either RB. Equation (1) suggests that the ϵ_{11} component of the rotated tensor is the most relevant in determining the extent of these PhP modes.

2.2 Hybridization of biaxial hyperbolic PhPs and SPPs

We examine the hybridization of SPPs of graphene with hyperbolic PhPs of α-MoO$_3$ via modulation of chemical potential (μ) in graphene. We consider a heterostructure having the configuration: air/graphene/α-MoO$_3$/silicon as shown in Figure 1(a) and explore the dispersion of polaritons, shown in Figure 2. The conductivity of graphene for various values of chemical potential is shown in Figure 1(c). For $\mu = 0.025$ and 0.05 eV, we observe smearing of hyperbolic PhP modes in all the RBs of α-MoO$_3$ (Figure 2(d)–(i)), however, there are no significant changes in the dispersion of hyperbolic PhPs in the plotted range of wave-vectors. This is due to interband transition in graphene upon excitation by a photon with an energy greater than 2μ (around 403 cm^{-1} and 806 cm^{-1} for $\mu = 0.025$ and 0.05 eV, respectively). At $\mu = 0.1$ eV in Figure 2(j), a broad mode is observed above the RB-3 spectral region and below the RB-2 spectral region. This mode corresponds to the SPPs of graphene, since as the chemical potential increases, the graphene plasmon dispersion moves closer to the light cone [28]. Due to the inherently lossy nature of the SPP mode, it is broader than the phonon modes. Furthermore, in Figure 2(k) and (l), a variation is observed in the dispersion of the fundamental mode of hyperbolic PhPs in the RB-1 spectral region. This is ascribed to the hybridization of hyperbolic PhPs of α-MoO$_3$ with SPPs of graphene forming HPPPs. Moreover, for $\mu = 0.3$ and 0.5 eV, the dispersion of hyperbolic PhPs in RB-1 and RB-2 spectral region become steeper compared to the no graphene case, which is a strong indication of hybridization of hyperbolic PhPs of α-MoO$_3$ with SPPs of graphene (Figure 2(m)–(r)). Additionally, we observe that the dispersion curve of SPPs becomes nearly horizontal as it approaches the TO phonon frequencies of α-MoO$_3$. This behaviour is due to the avoided-crossing [28, 30],

which suggests a coupling between surface plasmons of graphene and TO phonons of α-MoO$_3$ and further substantiates the formation of HPPPs. Dispersion curves in Figure 2(o) and (r) demonstrate that these hybrid modes can propagate outside the RB-1 and RB-2 spectral region, respectively, providing additional operational bandwidth compared to HPhPs of α-MoO$_3$ and relatively less losses compared to the SPPs of graphene.

Apart from fundamental modes of hyperbolic PhPs in RB-1 and RB-2, variation in the dispersion of higher-order PhP modes is observed upon integration of graphene. For a particular mode index (k_ρ/k_0), a blue-shift is observed in the frequencies of higher-order modes with increasing chemical potential of graphene, which we will discuss in the sections below. Similar to the observed trend in RB-1 and RB-2 spectral regions, hyperbolic PhP modes in the RB-3 spectral region are strongly dominated by graphene's interband transitions at lower μ values (0.025 and 0.05 eV) and graphene's SPPs at higher μ values. At $\mu = 0.3$ and 0.5 eV, mode repulsion is observed near the out-of-plane TO phonon frequency of α-MoO$_3$ which indicates the coupling of SPPs with these TO phonons. A discussion of the effect of thickness of α-MoO$_3$ on dispersion of HPPPs is presented in the Section S2 of supplementary information.

Hybridization of SPPs and hyperbolic PhPs is further investigated via iso-frequency surfaces for these polaritons, plotted as a function of ϕ, μ and k_ρ/k_0. We consider $\omega = 700$ cm^{-1}, 900 cm^{-1}, 960 cm^{-1} and 980 cm^{-1}, which are representative of frequencies in the RB-1, RB-2, transition region between RB-2 and RB-3, and RB-3 spectral regions in Figure 3. At $\omega = 700$ cm^{-1} in Figure 3(a), we observe that the fundamental and higher-order hyperbolic PhP modes of α-MoO$_3$ appear as hyperbolae aligned in the $\phi = 90°$ direction (i.e. y-direction). The iso-frequency surfaces of the heterostructure of α-MoO$_3$ and graphene with $\mu = 0.1$, 0.3, 0.5 eV appear as ellipses squeezed along $\phi = 90°$ due to the hybridization of hyperbolic PhPs of α-MoO$_3$ with the isotropic SPPs of graphene along y-direction. Furthermore, we observe a shift towards lower mode index in the first-order mode of hyperbolic PhPs with increasing chemical potential of graphene compared to that of no graphene (see Figure S5 of supplementary information). Figure 3a confirms that the higher order PhP modes are affected by graphene integration with α-MoO$_3$. For $\mu = 0.3$ and 0.5 eV, the SPP wave vector decreases resulting in smaller ellipses compared to the $\mu = 0.1$ eV case. Similarly, at $\omega = 900$ cm^{-1} in Figure 3(b), the hyperbola is found aligned along $\phi = 0°$ (x-direction) and first-order mode inside hyperbola varies with increasing chemical potential. These results confirm the presence of tunable hybridization of fundamental and

higher-order PhP modes with SPPs via chemical potential of graphene. Polar plots for other chemical potentials at $\omega = 700\,\mathrm{cm}^{-1}$ and $900\,\mathrm{cm}^{-1}$ are presented in the supplementary information. At $\omega = 960\,\mathrm{cm}^{-1}$, we do not observe hyperbolic PhP modes for the no graphene case in Figure 3(c). This is associated with the inherent dielectric response of α-MoO$_3$ in the transition from RB-2 to RB-3 spectral region. However, graphene SPPs dominate the formation of HPPPs for $\mu = 0.3$ and $0.5\,\mathrm{eV}$ as shown by the squeezed ellipse in Figures 3(c) and S6 of supplementary information. Moreover, at $\omega = 980\,\mathrm{cm}^{-1}$, we observe the transition of hyperbolic contour into an elliptical contour for the no graphene case as shown in Figure 3(d). For $\mu = 0.1\,\mathrm{eV}$, we observe that the elliptical contour is elongated along x-crystalline direction, which is attributed to mode repulsion between HPPP modes in the RB-2 and RB-3 spectral regions for $\phi = 0°$. As a result, we observe higher mode index at $980\,\mathrm{cm}^{-1}$ along x-direction. On the other hand, HPPP modes in the RB-2 spectral region do not exist for $\phi = 90°$ and consequently, we have a lower mode index at $980\,\mathrm{cm}^{-1}$ along y-direction as compared to the x-crystalline direction (see Figure S6 of supplementary information). Hence the elliptical contour for $\mu = 0.1\,\mathrm{eV}$ is elongated along x-crystal direction. Lastly, at $\mu = 0.3$ and $0.5\,\mathrm{eV}$, we observe a feeble elliptical contour in Figure S4 of supplementary information (which are absent in Figure 3(d)
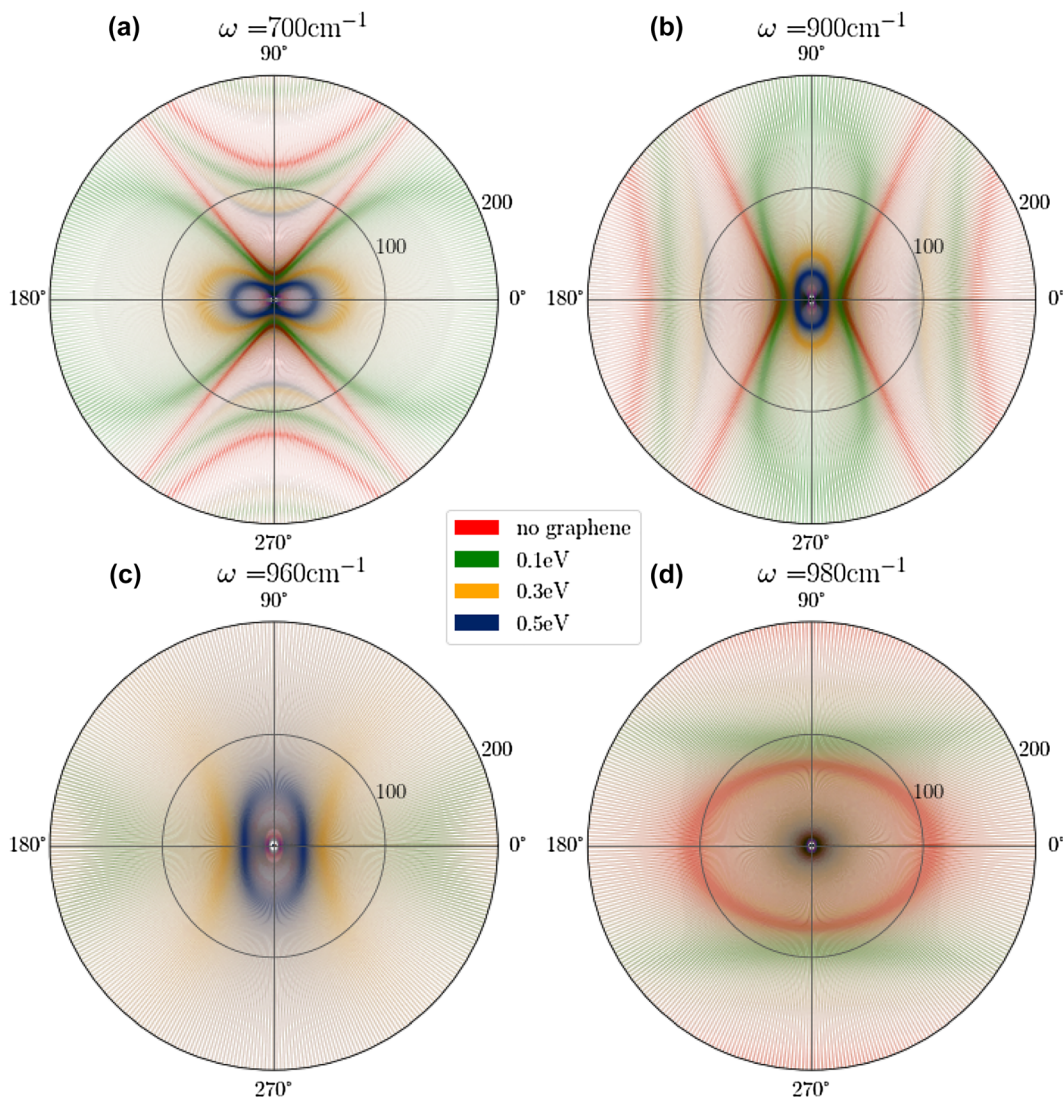
Figure 3: Polar plots of HPPP modes in 50 nm thin α-MoO$_3$ and graphene heterostructure as a function of graphene's chemical potential (0.1, 0.3, 0.5 eV): HPPP fundamental and first-order modes are represented by imaginary part of Fresnel's reflection coefficient for p-polarized light. Radial and azimuthal directions correspond to mode index (k_p/k_0) and ϕ, respectively. Effect of graphene's chemical potential on HPPP modes is demonstrated by green, orange and blue color for $\mu = 0.1$, 0.3, and 0.5 eV, respectively. The fringes at the edges of the polar plots are the artefact of the scatter type plotting scheme.

is due to relatively greater strength of contour for no graphene case). This can be attributed to type-1 HPPPs in the RB-3 spectral region. After integration of graphene with μ = 0.3 and 0.5 eV, the HPPP modes in the RB-3 spectral region move upward (or towards higher mode index) and create a spectral gap around 980 cm^{-1} (see Figures S4 and S6 of supplementary information), resulting in a feeble elliptical contour.

In order to understand the origin of this active tunability and the angle dependence of these hybrid modes, we derive an analytical expression for these dispersion relations under the quasistatic approximation ($k_\rho \gg k_0$). The expression for the dispersion curve then is given by:

$$\frac{k_\rho}{k_0}(\omega) = \frac{\psi}{k_0 d}\left[\tan^{-1}\left(\frac{\psi\left(\epsilon_1 + i\left(\frac{k_\rho}{k_0}\right)\sigma Z_0\right)}{\epsilon_z}\right) + \tan^{-1}\left(\frac{\epsilon_3 \psi}{\epsilon_z}\right) + n\pi\right] \quad (1)$$

Here, σ is the conductivity of graphene, $Z_0 = \sqrt{\mu_0/\epsilon_0}$ is the impedance of free space, ϵ_z is the z-direction (out of plane) permittivity of α-MoO$_3$ and $\psi = i\sqrt{\epsilon_z/\left(\epsilon_x \cos^2\phi + \epsilon_y \sin^2\phi\right)}$ and n is an integer. $\epsilon_1 = 1$ and $\epsilon_3 = 2.5$ are taken as the permittivities of the air and Si substrate, respectively. This expression can be derived by imposing the condition that the total of phase shift due to reflection at the two interfaces of the α-MoO$_3$ slab plus the propagation phase shift should be an integral multiple of 2π (see supplementary information). The variation of the graphene Fermi level through a gate voltage modifies σ which affects the reflection phase shift at that interface, thereby enabling the tunability of the hybrid modes. It must be noted that all the results presented in this work are full wave calculations without using the quasi-static approximation.
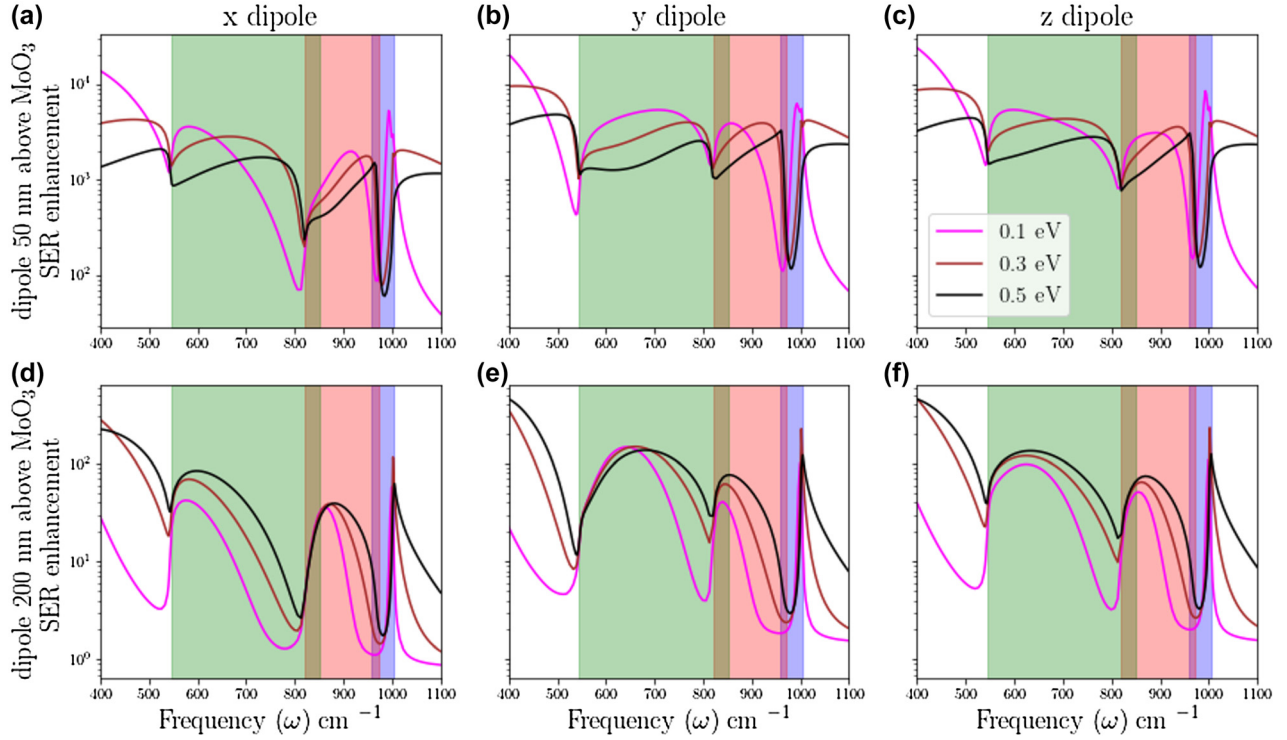
2.3 Anisotropic spontaneous emission via biaxial hybrid polaritons

Next, we explore the anisotropic SER enhancement from an electric dipole placed in the vicinity of graphene/α-MoO$_3$/Si heterostructure, as shown in Figure 1. To the best of our knowledge, anisotropic SERs for natural biaxial hyperbolic material have not been reported in the literature so far. Since α-MoO$_3$ exhibits in-plane hyperbolicity, we examine the anisotropic SERs by considering the polarization of the electric dipole along x-, y-, and z-directions. Distance of the electric dipole from the surface of the heterostructure (represented by z_0) is taken to be 50 and 200 nm, whereas μ is varied as 0.1 eV, 0.3 eV and 0.5 eV, as shown in Figure 4.

For comparison, we have also evaluated the anisotropic SERs through α-MoO$_3$ without graphene and for lower μ values, shown in the Section S4 of supplementary information. Integration of graphene with α-MoO$_3$ crystals not only provides tunable spontaneous emission but also enhances the SER to a much broader operational bandwidth.

At z_0 = 50 nm, the order of magnitude of SER is found to be more than 10^3 inside the RB spectral regions for x, y and z oriented dipoles as shown in Figure 4(a)–(c) respectively. Anisotropic SER spectra are dominated by graphene SPP modes outside the RBs of α-MoO$_3$. The difference between SER spectra in the RB spectral regions with and without integration of graphene and α-MoO$_3$ is associated with the formation of HPPPs, which provides a larger operational bandwidth. Variation of SER spectra in the RBs as a function of chemical potential is due to the change in the dispersion of HPPP modes with chemical potential, as discussed above. Spectral dips in SERs spectra are attributed to the spectral gap due to the absence of strongly confined SPP modes and hyperbolic PhP modes in the avoided crossing regions of the dispersion. Within such an avoided crossing, the dipole cannot couple to any mode effectively and hence spontaneous emission is suppressed. Here, we see that the line-widths of spectral dips decrease with increasing chemical potential, which is due to the fact that the graphene plasmon mode index decreases upon increase of chemical potential [28], decreasing the strength of the avoided crossing at larger mode indices just below the RBs of α-MoO$_3$. Moreover, a blue-shift in the spectral dip is observed from 960 cm^{-1}–980 cm^{-1} when μ increases from 0.1 to 0.3 eV. As described above with Figure 3(c) and (d), this is due to the shift of the RB-3 HPPPs towards higher mode index as the graphene Fermi level increases – this trend is opposite to that of the HPPPs in the other bands.

At z_0 = 200 nm, (shown in Figure 4(d)–(f)), we observe a decrease in the SER by one order of magnitude due to the evanescent nature of SPPs and HPPPs, resulting in reduced interaction of polaritonic modes with the electric dipole and hence reduction of the SERs. The dips in the SER spectra are due to the spectral gap of polariton modes, as discussed above. Reduction in the line-width of spectral dips with increasing chemical potential is found as expected. Below RB-1 spectral region, the SER for μ = 0.3 and 0.5 eV is higher in comparison with smaller μ values. Since higher chemical potential increases the imaginary part of the graphene conductivity, it reduces the confinement of SPPs. This can be seen from dispersion of SPPs in Figure 2, where one can observe SPP modes at higher μ values just below the RB-1 spectral region move to smaller k_ρ values. As a result, SPP modes for higher chemical potential have an evanescent tail at a larger distance away from the

Figure 4: Anisotropic spontaneous emission rates for dipole placed above air/graphene/α-MoO$_3$ (50 nm)/Si heterostructure: (a)–(c) represent SER enhancements at different μ values for x-, y-and z-polarized electric dipole, respectively, at $z_0 = 50$ nm. (d)–(f) represent SER enhancements at different μ values for x-, y- and z-polarized electric dipole, respectively, at $z_0 = 200$ nm. The green, red and blue shaded regions represent the RB-1, RB-2, and RB-3 spectral regions of α-MoO$_3$, respectively.

surface compared to the SPP modes for smaller chemical potential and hence the SER can be enhanced. A mathematical justification can further be provided based on the envelope $k_\rho^2 e^{-2k_\rho z_0}$ which peaks at $k_\rho \sim 1/z_0$. So depending on whether the mode is resonant at $k_\rho \sim 1/z_0$, one can observe an increase in the SER. The variation of the anisotropic SER spectra as a function of the thickness of α-MoO$_3$ is discussed in the Section S4 of the supplementary information. Similarly, spontaneous emission spectra for the air/graphene/Si heterostructure are discussed in Section S5 of the supplementary information. These SER spectra substantiate our claim that one can observe a remarkable spontaneous emission enhancement for an electric dipole in the vicinity of α-MoO$_3$ integrated with graphene over a broad spectral range.

2.4 Application to valley quantum interference

We demonstrate the power of such a tunable anisotropic SER for application in spontaneous valley coherence [16].

Quantum coherence in solid state systems is important not only from a fundamental point of view but is a key ingredient for realizing the promised applications in quantum technologies like quantum computing [47], quantum key distribution [48] and quantum metrology [49]. In the infrared range, gapped Dirac systems [50, 51] such as biased bilayer graphene [52, 53] and similar systems could serve as an important excitonic building block for such technologies. The electronic bandstructure of these systems consists of two degenerate valleys K and K', in which the optical selection rule is sensitive to the polarization ($\sigma^\pm$) of the photon. In order to harness this "valley degree of freedom", it is important to be able to actively control the coherence between excitons in the two valleys. While this coherence has been demonstrated in the stimulated regime [54], where the valley excitons inherit coherence from the exciting laser, a spontaneous route to such coherence generation would greatly simplify the device architecture. Such a spontaneous route to valley coherence has been previously demonstrated using structured metamaterials [44]. Our graphene/MoO$_3$ heterostructure would allow for easy fabrication and enable electrostatic control of valley

coherence, which could be easily implemented on a chip and provide a low-cost, facile fabrication and chip-scale alternatives for building relevant technologies.

Valley coherence can be quantified experimentally using the degree of linear polarization or DoLP of the emission, where DoLP = $(I_X - I_Y)/(I_X + I_Y)$, I_X and I_Y being the intensities of the two linearly polarized emissions. It can easily be shown that in the presence of a weak pump, the DoLP is approximately equal to the quantum interference Q, which is defined as [16, 44]:

$$Q = \frac{\gamma_x - \gamma_y}{\gamma_x + \gamma_y} \tag{2}$$

where γ_x and γ_y are the Purcell factors for x and y polarized dipoles, respectively. The valley quantum interference is proportional to the anisotropy between the Purcell factors for orthogonal dipoles. The geometrical configuration for this experiment would involve a gapped Dirac system such as a bilayer graphene system placed a certain distance away from the monolayer graphene/α-MoO$_3$ system. The exciton of this gapped Dirac system will be represented by the dipole. The quantum interference for this heterostructure with a 50 nm thick α-MoO$_3$ layer is plotted as a function of frequency for various values of chemical potential μ of graphene in Figure 5. Since α-MoO$_3$ is a naturally biaxial material, we observe large magnitude of quantum interference in RB-1 and RB-2 spectral regions, where dipole is aligned along the y- and x-crystallographic axes, respectively, and can couple more strongly to PhP modes as compared to the dipole polarized orthogonal to the metallic direction of the hyperbolic crystal.

Integration of graphene at chemical potentials of 0.025 and 0.05 eV suppresses the quantum interference, as for the chosen dipole distances, the emitter does not couple efficiently to the HPPPs as they occur at very large wave vectors (as seen in Figure 2) following the relation $k_\rho \sim 1/z_0$ and the graphene itself is isotropic. However, when the chemical potential is changed to 0.1 eV, 0.3 eV and 0.5 eV, we begin to see significant differences in the quantum interference, due to coupling with the HPPP modes. For $z_0 = 50$ nm, we see large positive quantum interference just below 545 cm^{-1}. This is explained by the avoided crossing between the graphene plasmon and phonon polaritons in RB-1 region, when the plane of propagation is along y–z plane (i.e. $\phi = 90°$). However, this phenomenon does not occur in the x–z plane (i.e. $\phi = 0°$) for frequencies below RB-1. Thus, the y-dipole sees an avoided crossing unlike the x dipole, and we get large positive quantum interference. Furthermore, a shift in the frequency band of large quantum interference is observed with increasing chemical potential of graphene from 0.025 to 0.5 eV inside RB-1 and RB-2 spectral region which is due to active tuning of HPPP modes, as discussed above.

Moreover, for $z_0 = 200$ nm, we observe a similar phenomenon at $\mu = 0.1$–0.5 eV. As we increase μ, the SPPs mode moves to a lower k_ρ/k_0. Since large k_ρ/k_0 modes are tightly confined, they remain unavailable to dipoles placed far away from heterostructure. Hence, this lower wave-vector modes at large μ are more prominent for a dipole at $z_0 = 200$ nm as can be observed in Figure 5(b). We also observe that the frequency corresponding to large negative quantum interference shifts at the upper end of the RB-1 which, as described above, is due to the direction dependent avoided crossing at the lower end of the RB-2 for one emitter polarization as opposed to coupling with the isotropic graphene SPP outside the RB-1 for the other
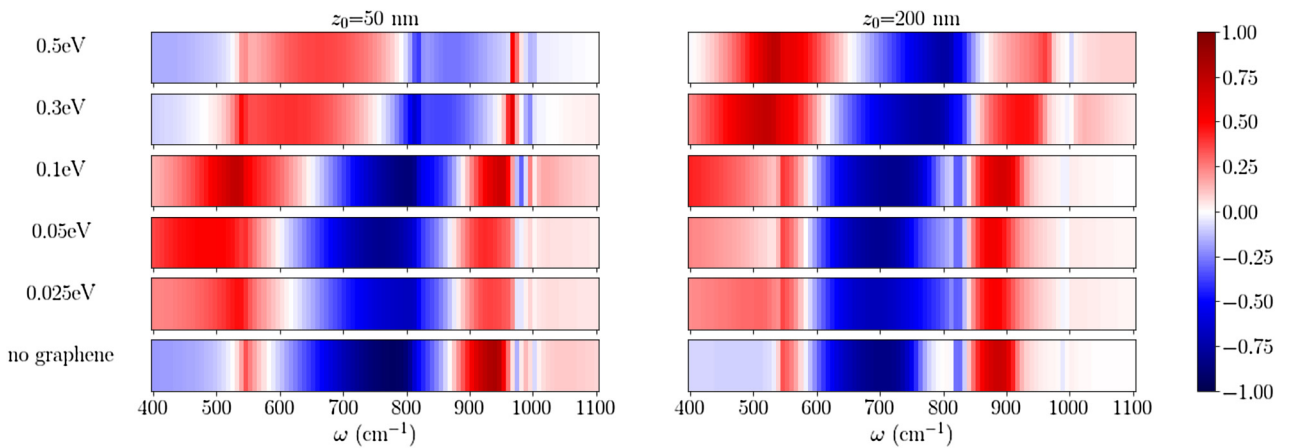
Figure 5: Quantum interference (Q) for air/graphene/MoO$_3$/Si heterostructure with MoO$_3$ thickness of 50 nm, plotted as a function of frequency, for two different dipole heights of $z_0 = 50$ and 200 nm, respectively. The color bar represents unitless quantity quantum interference (Q).

polarization. Thus, we see a large value of negative quantum interference just below RB-2, instead of a nearly zero value after RB-1. We also see that the large negative quantum interference for most of the RB-1 region in the no graphene case is replaced by a small positive quantum interference when 0.3 eV or 0.5 eV graphene is introduced. This can be understood from Figure 3 where we observe that while there are no available modes in x-direction without graphene (hyperbola), the lemniscate shape of the fundamental HPPP mode with μ = 0.3 and 0.5 eV for graphene provides available modes to both dipole orientations. We also see a corresponding reverse phenomenon in RB-2 region in Figure 5, which has a similar explanation.

In summary, we observe that our proposed platform provides a convenient way to achieve electrostatically tunable quantum interference in a valley exciton material placed nearby via formation of anisotropic hybrid plasmon-phonon polariton modes which couple selectively with dipoles oriented along x- and y-direction.

3 Conclusions

In conclusion, we have investigated the integration of graphene with recently discovered biaxial hyperbolic vdW crystal of α-MoO$_3$ for applications in quantum photonics. We found a unique direction dependent hybridization of surface plasmon-polaritons of graphene with fundamental and higher-order modes of hyperbolic phonon polaritons in α-MoO$_3$ crystals forming hybrid plasmon phonon polaritons. We show that these HPPPs can be actively tuned via electrostatic gating of graphene and can exist outside the RBs of α-MoO$_3$, providing enhanced operational bandwidth. We have found significantly large anisotropic SER enhancements of more than 10^3 in the vicinity of the proposed heterostructure with an operational bandwidth from 400 cm^{-1}–1100 cm^{-1} and report large and actively tunable quantum interference for SER.

Compared to uniaxial hyperbolic materials, the tunable biaxial hyperbolic heterostructure proposed in this work has unique advantages in terms of strong in-plane anisotropy leading to precise control of energy channeling direction. The current platform also overcomes the issue of complex lithographic fabrication for schemes implementing biaxial hyperbolicity through metasurfaces [55] since our platform relies on the intrinsic phononic and plasmonic response of the constituent materials of the heterostructure. This heterostructure also provides an interesting case for the study of exceptional point physics [56]. The

tunability of the isofrequency surfaces of the HPPP modes could find application in tunable radiative heat flow control including radiative cooling and exotic phenomenon such as tunable super-Planckian near-field thermal emission [57–60]. The broadband and strong light–matter interaction enabled by these heterostructure could be a powerful tool for vibrational spectroscopy particularly for biosensing, where electrostatic gating could enable not only high sensitivity and tunable spectral selectivity [61–63] but also serve as a unique probe of orientation of the molecule due to the in-plane hyperbolic nature of the HPPPs in our heterostructures. Our work opens new avenues for tunable in-plane hyperbolic polaritonics for other exotic applications in quantum interference [16, 44, 45, 64–66], gate tunable planar refraction devices using polaritons [67], emission pattern engineering [68], quantum field entanglement [69], engineering interaction between multiple quantum emitters [70–72] and Kerr nonlinearity enhancement [17].

Note: After the submission of our manuscript, these recent related works were brought to our notice [73, 74].

4 Methods

Model for calculation of polariton dispersion

We used the standard expression for complex valued 2D graphene conductivity derived from the local limit of the random phase approximation [30, 75]

$$
\begin{aligned}
\sigma(\Omega,\mu) &= \frac{ie^2 k_B T}{\pi\hbar^2(\Omega + i/\tau)} \\
&\times \left[\frac{\mu}{k_B T} + 2\ln\left(\exp\left(-\frac{\mu}{k_B T}\right) + 1\right)\right] \\
&+ \frac{ie^2}{4\pi\hbar}\ln\left(\frac{2\mu - \hbar(\Omega + i/\tau)}{2\mu + \hbar(\Omega + i/\tau)}\right)
\end{aligned}
\tag{3}
$$

Here, the first-term represents the intraband contribution to graphene conductivity and the second term is the interband contribution. e, k_B and $\hbar$ refer to the charge of electron, Boltzmann's constant and reduced Planck constant, respectively. We considered the value of temperature as T = 300 K and relaxation time $\tau = 10^{-13}$ s which matches well with experimental results [75]. Here μ refers to the and the chemical potential of graphene chosen (in eV). $\Omega = 200\pi c\omega$ is the angular frequency in rad/s (where ω is the frequency in cm^{-1}). This conductivity expression has been plotted for various chemical potentials (μ) in the supplementary document (Figure S1). Dielectric permittivity of graphene is derived using the Drude model to be [76]

$$
\epsilon_{gr} = 1 + \frac{i\sigma(\omega,\mu)}{\epsilon_0 \omega d}
\tag{4}
$$

where ϵ_{gr} is the relative permittivity of graphene in the in-plane directions, ϵ_0 is the permittivity of free space, and the thickness of the

	x	*y*	*z*
ϵ_∞	4.0	5.2	2.4
ω_{LO} (cm^{-1})	972	851	1004
ω_{TO} (cm^{-1})	820	545	958
γ (cm^{-1})	4	4	2

monolayer graphene (d) is taken 0.34 nm in accordance with experimental results [77]. Since the out-of-plane conductivity of graphene is zero, the relative permittivity of graphene in the out-of-plane direction is unity.

The permittivity of α-MoO$_3$ in mid-IR spectral region is given by the Lorentz oscillator model. Frequency-dependent dielectric permittivity along each crystal axis is written as

$$\epsilon_i(\omega) = \epsilon_{\infty,i}\left(1 + \frac{\omega_{LO,i}^2 - \omega_{TO,i}^2}{\omega_{TO,i}^2 - \omega^2 - i\gamma_i\omega}\right) \tag{5}$$

The Table shows the values we used for the parameters ϵ_∞, ω_{LO}, ω_{TO} and γ along each principal axis, as proposed in [46].

The respective expressions for permittivities along principal directions are plotted in the supplementary information (Figure S1).

Permittivity tensor for any particular plane of propagation (i.e. for any ϕ) is obtained from $\epsilon(\phi, \omega) = R(\phi)\epsilon_{principal}(\omega)R^T(\phi)$ where

$$R(\phi) = \begin{pmatrix} \cos\phi & -\sin\phi & 0 \\ \sin\phi & \cos\phi & 0 \\ 0 & 0 & 1 \end{pmatrix} \tag{6}$$

is the rotation matrix for transformation of coordinate system, and $\epsilon_{principal}(\omega)$ is the permittivity tensor in principle axis coordinate system [40]. This leads to the final expression

$$\epsilon(\phi,\omega) = \begin{pmatrix} \epsilon_x\cos^2\phi + \epsilon_y\sin^2\phi & \sin\phi\cos\phi(\epsilon_y - \epsilon_x) & 0 \\ \sin\phi\cos\phi(\epsilon_y - \epsilon_x) & \epsilon_x\sin^2\phi + \epsilon_y\cos^2\phi & 0 \\ 0 & 0 & \epsilon_z \end{pmatrix}$$

Fresnel's reflection coefficient for p-polarized light is evaluated from well-known 4×4 transfer matrix method [40].

Calculation of Purcell factor

Purcell factor for an emitter placed at a height z_0 above a surface in terms of the Green's Dyadic function can be written as [41–43]

$$\gamma = \frac{P}{P_0} = 1 + \frac{6\pi}{k_0}\overrightarrow{\mu} \cdot \text{Im}(G) \cdot \overrightarrow{\mu} \tag{7}$$

where $\overrightarrow{\mu}$ is a unit vector along the direction of the dipole, $G = G(\overrightarrow{r_0}, \overrightarrow{r_0})$ is the scattering part of the Green's dyadic function at the position of the dipole, and $k_0 = \frac{\omega}{c}$. Here, P and P_0 are the spontaneous emission rates of a dipole placed above the heterostructure and in free space, respectively.

From [41, 43] we can express the Green's tensor as

$$G = \frac{i}{8\pi^2} \iint (r_{ss}M_{ss} + r_{sp}M_{sp} + r_{ps}M_{ps} + r_{pp}M_{pp})e^{2ik_z z_0}dk_x dk_y \tag{8}$$

where the integral is taken over all space and 'M' matrices are given by:

$$M_{ss} = \frac{1}{k_z k_\rho^2}\begin{pmatrix} k_y^2 & -k_x k_y & 0 \\ -k_x k_y & k_x^2 & 0 \\ 0 & 0 & 0 \end{pmatrix}$$

$$M_{sp} = \frac{1}{k_0 k_\rho^2}\begin{pmatrix} -k_x k_y & -k_y^2 & -\frac{k_y k_\rho^2}{k_z} \\ k_x^2 & k_x k_y & \frac{k_x k_\rho^2}{k_z} \\ 0 & 0 & 0 \end{pmatrix}$$

$$M_{ps} = \frac{1}{k_0 k_\rho^2}\begin{pmatrix} k_x k_y & -k_x^2 & 0 \\ k_y^2 & -k_x k_y & 0 \\ -\frac{k_y k_\rho^2}{k_z} & \frac{k_x k_\rho^2}{k_z} & 0 \end{pmatrix}$$

$$M_{pp} = \frac{k_z}{k_0^2 k_\rho^2}\begin{pmatrix} -k_x^2 & -k_x k_y & -\frac{k_x k_\rho^2}{k_z} \\ -k_x k_y & -k_y^2 & -\frac{k_y k_\rho^2}{k_z} \\ \frac{k_x k_\rho^2}{k_z} & \frac{k_y k_\rho^2}{k_z} & \frac{k_\rho^4}{k_z^2} \end{pmatrix}$$

From here, we can recast the integral in polar coordinates and calculate the spontaneous emission rate enhancements.

References

[1] T. Low, A. Chaves, J. D. Caldwell, et al., "Polaritons in layered two-dimensional materials," *Nat. Mater.*, vol. 16, pp. 182–194, 2016.

[2] D. N. Basov, M. M. Fogler, and F. J. G. de Abajo, "Polaritons in van der waals materials," *Science*, vol. 354, pp. aag1992, 2016.

[3] A. Reserbat-Plantey, I. Epstein, I. Torre, et al., "Quantum nanophotonics in two-dimensional materials," *ACS Photonics*, vol. 8, pp. 85–101, 2021.

[4] W. Ma, P. Alonso-González, S. Li, et al., "In-plane anisotropic and ultra-low-loss polaritons in a natural van der waals crystal," *Nature*, vol. 562, pp. 557–562, 2018.

[5] J. Taboada-Gutiérrez, G. Álvarez-Pérez, J. Duan, et al., "Broad spectral tuning of ultra-low-loss polaritons in a van der waals crystal by intercalation," *Nat. Mater.*, vol. 19, pp. 964–968, 2020.

[6] S. Dixit, N. R. Sahoo, A. Mall, and A. Kumar, "Mid infrared polarization engineering via sub-wavelength biaxial hyperbolic van der waals crystals," *Sci. Rep.*, vol. 11, pp. 1–9, 2021.

[7] N. R. Sahoo, S. Dixit, A. K. Singh, S. H. Nam, N. X. Fang, and A. Kumar, "High temperature mid-IR polarizer via natural in-plane hyperbolic van der waals crystals," *Adv. Opt. Mater.*, p. 2101919, 2021. https://doi.org/10.1002/adom.202101919.

[8] H. Yang, H. Jussila, A. Autere, et al., "Optical waveplates based on birefringence of anisotropic two-dimensional layered materials," *ACS Photonics*, vol. 4, pp. 3023–3030, 2017.

[9] R.-J. Shiue, Y. Gao, C. Tan, et al., "Thermal radiation control from hot graphene electrons coupled to a photonic crystal nanocavity," *Nat. Commun.*, vol. 10, 2019. https://doi.org/10.1038/s41467-018-08047-3.

[10] M. L. Andersen, S. Stobbe, A. S. Sørensen, and P. Lodahl, "Strongly modified plasmon–matter interaction with mesoscopic quantum emitters," *Nat. Phys.*, vol. 7, pp. 215–218, 2010.

[11] X. Liu and M. C. Hersam, "2d materials for quantum information science," *Nat. Rev. Mater.*, vol. 4, pp. 669–684, 2019.

[12] H. Chen, F. Zhang, D. Zhao, et al., "Surface-plasmon-enhanced quantum field entanglement through anisotropic Purcell factors," *Phys. Rev.*, vol. 96, pp. 043865–043875, 2017.

[13] Y. Gu, L. Wang, P. Ren, et al., "Surface-plasmon-induced modification on the spontaneous emission spectrum via subwavelength-confined anisotropic Purcell factor," *Nano Lett.*, vol. 12, pp. 2488–2493, 2012.

[14] E. M. Purcell, H. C. Torrey, and R. V. Pound, "Resonance absorption by nuclear magnetic moments in a solid," *Phys. Rev.*, vol. 69, pp. 37–38, 1946.

[15] Y.-S. Lee and S.-D. Lin, "Polarized emission of quantum dots in microcavity and anisotropic Purcell factors," *Opt. Express*, vol. 22, p. 1512, 2014.

[16] M. Nalabothula, P. Jha, T. Low, and A. Kumar, "Engineering valley quantum interference in anisotropic van der waals heterostructures," *Phys. Rev. B*, vol. 102, 2020, Art no. 045416.

[17] H. Chen, J. Ren, Y. Gu, D. Zhao, J. Zhang, and Q. Gong, "Nanoscale kerr nonlinearity enhancement using spontaneously generated coherence in plasmonic nanocavity," *Sci. Rep.*, vol. 5, 2015. https://doi.org/10.1038/srep18315.

[18] K.-D. Park, T. Jiang, G. Clark, X. Xu, and M. B. Raschke, "Radiative control of dark excitons at room temperature by nano-optical antenna-tip Purcell effect," *Nat. Nanotechnol.*, vol. 13, pp. 59–64, 2017.

[19] L. Eswaramoorthy, S. Mokkapati, and A. Kumar, "Engineering Purcell factor anisotropy for dark and bright excitons in two dimensional semiconductors," *J. Phys. D: Appl. Phys.*, vol. 55, p. 225103, 2022.

[20] Z. Guo, H. Jiang, and H. Chen, "Hyperbolic metamaterials: from dispersion manipulation to applications," *J. Appl. Phys.*, vol. 127, 2020, Art no. 071101.

[21] J. Zhou, T. Koschny, M. Kafesaki, and C. M. Soukoulis, "Negative refractive index response of weakly and strongly coupled optical metamaterials," *Phys. Rev. B*, vol. 80, 2009, Art no. 035109.

[22] M. N. Gjerding, R. Petersen, T. G. Pedersen, N. A. Mortensen, and K. S. Thygesen, "Layered van der waals crystals with hyperbolic light dispersion," *Nat. Commun.*, vol. 8, 2017. https://doi.org/10.1038/s41467-017-00412-y.

[23] J. Chen, M. Badioli, P. Alonso-González, et al., "Optical nano-imaging of gate-tunable graphene plasmons," *Nature*, vol. 487, pp. 77–81, 2012.

[24] M. Jablan, H. Buljan, and M. Soljačić, "Plasmonics in graphene at infrared frequencies," *Phys. Rev. B*, vol. 80, p. 245435, 2009.

[25] T. Low and P. Avouris, "Graphene plasmonics for terahertz to mid-infrared applications," *ACS Nano*, vol. 8, pp. 1086–1101, 2014.

[26] G. Hu, J. Shen, C.-W. Qiu, A. Alù, and S. Dai, "Phonon polaritons and hyperbolic response in van der waals materials," *Adv. Opt. Mater.*, vol. 8, p. 1901393, 2019.

[27] A. Woessner, M. B. Lundeberg, Y. Gao, et al., "Highly confined low-loss plasmons in graphene–boron nitride heterostructures," *Nat. Mater.*, vol. 14, pp. 421–425, 2014.

[28] A. Kumar, T. Low, K. H. Fung, P. Avouris, and N. X. Fang, "Tunable light–matter interaction and the role of hyperbolicity in graphene–hBN system," *Nano Lett.*, vol. 15, pp. 3172–3180, 2015.

[29] F. C. B. Maia, B. T. O'Callahan, A. R. Cadore, et al., "Anisotropic flow control and gate modulation of hybrid phonon-polaritons," *Nano Lett.*, vol. 19, pp. 708–715, 2019.

[30] D. T. Debu, F. T. Ladani, D. French, S. J. Bauman, and J. B. Herzog, "Hyperbolic plasmon–phonon dispersion on group velocity reversal and tunable spontaneous emission in graphene–ferroelectric substrate," *npj 2D Mater. Appl.*, vol. 3, 2019. https://doi.org/10.1038/s41699-019-0112-8.

[31] K. Zhou, L. Lu, B. Li, and Q. Cheng, "Hyperbolic plasmon–phonon dispersion and tunable spontaneous emission enhancement in ge2sb2te5-based multilayer graphene and hBN system," *J. Appl. Phys.*, vol. 130, 2021, Art no. 093102.

[32] S. Dai, Q. Ma, M. K. Liu, et al., "Graphene on hexagonal boron nitride as a tunable hyperbolic metamaterial," *Nat. Nanotechnol.*, vol. 10, pp. 682–686, 2015.

[33] Q. Zhang, Z. Zhen, Y. Yang, G. Gan, D. Jariwala, and X. Cui, "Hybrid phonon-polaritons at atomically-thin van der waals heterointerfaces for infrared optical modulation," *Opt. Express*, vol. 27, pp. 18585–18600, 2019.

[34] Q. Zhang, Z. Zhen, Y. Yang, G. Gan, D. Jariwala, and X. Cui, "Negative refraction inspired polariton lens in van der waals lateral heterojunctions," *Appl. Phys. Lett.*, vol. 114, p. 221101, 2019.

[35] Q. Zhang, Z. Zhen, C. Liu, D. Jariwala, and X. Cui, "Gate-tunable polariton superlens in 2d/3d heterostructures," *Opt. Express*, vol. 27, pp. 18628–18641, 2019.

[36] S. V. Morozov, V. V. Rumyantsev, A. V. Antonov, et al., "Efficient long wavelength interband photoluminescence from HgCdTe epitaxial films at wavelengths up to 26 μm," *Appl. Phys. Lett.*, vol. 104, 2014, Art no. 072102.

[37] V. Rumyantsev, M. Fadeev, V. Aleshkin, et al., "Carrier recombination, long-wavelength photoluminescence, and stimulated emission in HgCdTe quantum well heterostructures," *Phys. Status Solidi*, vol. 256, p. 1800546, 2019.

[38] I. Lyubomirsky, Q. Hu, and M. R. Melloch, "Measurement of far-infrared intersubband spontaneous emission from optically pumped quantum wells," *Appl. Phys. Lett.*, vol. 73, pp. 3043–3045, 1998.

[39] K. Donovan, P. Harrison, and R. W. Kelsall, "Stark ladders as tunable far-infrared emitters," *J. Appl. Phys.*, vol. 84, pp. 5175–5179, 1998.

[40] M. Schubert, "Polarization-dependent optical parameters of arbitrarily anisotropic homogeneous layered systems," *Phys. Rev. B*, vol. 53, pp. 4265–4274, 1996.

[41] A. Lakhtakia, "Green's functions and brewster condition for a halfspace bounded by an anisotropic impedance plane," *Int. J. Infrared Millimet. Waves*, vol. 13, pp. 161–170, 1992.

[42] L. Novotny and B. Hecht, *Principles of Nano-Optics*, UK, Cambridge University Press, 2012.

[43] J. Gomez-Diaz, M. Tymchenko, and A. Alù, "Hyperbolic metasurfaces: surface plasmons, light-matter interactions, and physical implementation using graphene strips," *Opt. Mater. Express*, vol. 5, pp. 2313–2329, 2015.

[44] P. K. Jha, N. Shitrit, X. Ren, Y. Wang, and X. Zhang, "Spontaneous exciton valley coherence in transition metal dichalcogenide monolayers interfaced with an anisotropic metasurface," *Phys. Rev. Lett.*, vol. 121, p. 116102, 2018.

[45] M. Sohoni, P. K. Jha, M. Nalabothula, and A. Kumar, "Interlayer exciton valleytronics in bilayer heterostructures interfaced with a phase gradient metasurface," *Appl. Phys. Lett.*, vol. 117, p. 121101, 2020.

[46] Z. Zheng, N. Xu, S. L. Oscurato, et al., "A mid-infrared biaxial hyperbolic van der waals crystal," *Sci. Adv.*, vol. 5, 2019, Art no. eaav8690.

[47] E. Knill, R. Laflamme, and G. J. Milburn, "A scheme for efficient quantum computation with linear optics," *Nature*, vol. 409, pp. 46–52, 2001.

[48] N. Gisin, G. Ribordy, W. Tittel, and H. Zbinden, "Quantum cryptography," *Rev. Mod. Phys.*, vol. 74, p. 145, 2002.

[49] V. Giovannetti, S. Lloyd, and L. Maccone, "Advances in quantum metrology," *Nat. Photonics*, vol. 5, pp. 222–229, 2011.

[50] Y. D. Lensky, J. C. W. Song, P. Samutpraphoot, and L. S. Levitov, "Topological valley currents in gapped Dirac materials," *Phys. Rev. Lett.*, vol. 114, p. 256601, 2015.

[51] A. Kumar, A. Nemilentsau, K. H. Fung, G. Hanson, N. X. Fang, and T. Low, "Chiral plasmon in gapped Dirac systems," *Phys. Rev. B*, vol. 93, 2016, Art no. 041413.

[52] L. Ju, L. Wang, T. Cao, et al., "Tunable excitons in bilayer graphene," *Science*, vol. 358, pp. 907–910, 2017.

[53] J. C. G. Henriques, I. Epstein, and N. M. R. Peres, "Absorption and optical selection rules of tunable excitons in biased bilayer graphene," *Phys. Rev. B*, vol. 105, pp. 045411–045419, 2022.

[54] A. M. Jones, H. Yu, N. J. Ghimire, et al., "Optical generation of excitonic valley coherence in monolayer WSe2," *Nat. Nanotechnol.*, vol. 8, pp. 634–638, 2013.

[55] J. S. Gomez-Diaz and A. Alù, "Flatland optics with hyperbolic metasurfaces," *ACS Photonics*, vol. 3, pp. 2211–2224, 2016.

[56] S. H. Park, S. Xia, S.-H. Oh, P. Avouris, and T. Low, "Accessing the exceptional points in a graphene plasmon–vibrational mode coupled system," *ACS Photonics*, vol. 8, pp. 3241–3248, 2021.

[57] X. Wang, R. Starko-Bowes, C. Khandekar, and Z. Jacob, "High-temperature thermal photonics," *Annu. Rev. Heat Transfer*, vol. 23, pp. 355–395, 2020.

[58] Y. Guo and Z. Jacob, "Thermal hyperbolic metamaterials," *Opt. Express*, vol. 21, p. 15014, 2013.

[59] Y. Guo, C. L. Cortes, S. Molesky, and Z. Jacob, "Broadband super-planckian thermal emission from hyperbolic metamaterials," *Appl. Phys. Lett.*, vol. 101, p. 131106, 2012.

[60] X. Wu and R. Liu, "Near-field radiative heat transfer between graphene covered biaxial hyperbolic materials," *ES Energy Environ.*, vol. 10, pp. 66–72, 2020.

[61] D. Rodrigo, O. Limaj, D. Janner, et al., "Mid-infrared plasmonic biosensing with graphene," *Science*, vol. 349, pp. 165–168, 2015.

[62] Y. Hu, Á. I. López-Lorente, and B. Mizaikoff, "Graphene-based surface enhanced vibrational spectroscopy: recent developments, challenges, and applications," *ACS Photonics*, vol. 6, pp. 2182–2197, 2019.

[63] S.-H. Oh, H. Altug, X. Jin, et al., "Nanophotonic biosensors harnessing van der waals materials," *Nat. Commun.*, vol. 12, 2021. https://doi.org/10.1038/s41467-021-23564-4.

[64] I. Thanopulos, V. Yannopapas, and E. Paspalakis, "Non-Markovian dynamics in plasmon-induced spontaneous emission interference," *Phys. Rev. B*, vol. 95, 2017, Art no. 075412.

[65] E. Lassalle, P. Lalanne, S. Aljunid, et al., "Long-lifetime coherence in a quantum emitter induced by a metasurface," *Phys. Rev. A*, vol. 101, 2020, Art no. 013837.

[66] V. Karanikolas and E. Paspalakis, "Plasmon-induced quantum interference near carbon nanostructures," *J. Phys. Chem. C*, vol. 122, pp. 14788–14795, 2018.

[67] J. Duan, G. Álvarez-Pérez, A. I. F. Tresguerres-Mata, et al., "Planar refraction and lensing of highly confined polaritons in anisotropic media," *Nat. Commun.*, vol. 12, 2021. https://doi.org/10.1038/s41467-021-24599-3.

[68] P. Zhang, P.-L. Ren, and X.-W. Chen, "On the emission pattern of nanoscopic emitters in planar anisotropic matrix and nanoantenna structures," *Nanoscale*, vol. 11, pp. 11195–11201, 2019.

[69] H. Chen, F. Zhang, D. Zhao, et al., "Surface-plasmon-enhanced quantum field entanglement through anisotropic Purcell factors," *Phys. Rev. A*, vol. 96, 2017, Art no. 043865.

[70] W. D. Newman, C. L. Cortes, A. Afshar, et al., "Observation of long-range dipole-dipole interactions in hyperbolic metamaterials," *Sci. Adv.*, vol. 4, p. eaar5278, 2018.

[71] C. L. Cortes and Z. Jacob, "Fundamental figures of merit for engineering förster resonance energy transfer," *Opt. Express*, vol. 26, p. 19371, 2018.

[72] C. L. Cortes and Z. Jacob, "Super-coulombic atom–atom interactions in hyperbolic media," *Nat. Commun.*, vol. 8, pp. 1–8, 2017.

[73] A. Yadav, R. Kumari, S. K. Varshney, and B. Lahiri, "Tunable phonon-plasmon hybridization in α- moo_3-graphene based van der Waals heterostructures," *Opt. Express*, vol. 29, pp. 33171–33183, 2021.

[74] G. Álvarez Pérez, A. González-Morán, N. Capote-Robayna, et al., "Active tuning of highly anisotropic phonon polaritons in van der Waals crystal slabs by gated graphene," *ACS Photonics*, vol. 9, pp. 383–390, 2021.

[75] F. H. L. Koppens, D. E. Chang, and F. J. G. de Abajo, "Graphene plasmonics: a platform for strong light–matter interactions," *Nano Lett.*, vol. 11, pp. 3370–3377, 2011.

[76] Y. Wu, Y. Wu, K. Kang, et al., "Characterization of CVD graphene permittivity and conductivity in micro-/millimeter wave frequency range," *AIP Adv.*, vol. 6, 2016, Art no. 095014.

[77] Y. R. Jang, K. Y. Kim, and K. H. Yoo, "Accurate measurement of thickness of large-area graphene layers by neutron reflectometry," *J. Mater. Sci.*, vol. 51, pp. 10059–10065, 2016.